PAPER

Check for updates

Enhanced supercapacitor performance of a Cu-Fe₂O₃/g-C₃N₄ composite material: synthesis, characterization, and electrochemical analysis†

Chetan Harak,[ad] Vinayak Kadam,[b] Rakhamaji Gavhane,[c] Sagar Balgude, [ID][a] Anil Rakshe,[d] Neha Brahmankar,[e] Santosh Uke, [ID][e] Dilip Satpute,*[a] Hari Pawar [ID] *[a] and Satish Mardikar[f]

A Cu-doped Fe₂O₃/g-C₃N₄ composite, synthesized *via* a straightforward hydrothermal process with controlled morphologies, represents a significant advancement in supercapacitor electrode materials. This study systematically analyzes the impact of Cu doping in Fe₂O₃ and its synergistic combination with g-C₃N₄ to understand their influence on the electrochemical performance of the resulting composite, focusing on Cu doping in Fe₂O₃ rather than varying Fe₂O₃/g-C₃N₄ content. The comprehensive characterization of these composites involved a suite of physicochemical techniques. X-ray diffraction (XRD) confirmed the successful synthesis of the composite, while field emission scanning electron microscopy (FESEM) and transmission electron microscopy (TEM) were employed to investigate the morphological attributes of the synthesized materials. X-ray photoelectron spectroscopy (XPS) spectra confirmed the elemental composition of the composite with 6% Cu doped Fe₂O₃/g-C₃N₄. The composite electrode, which incorporated 6% Cu doped Fe₂O₃ with g-C₃N₄, exhibited exceptional cycling stability, retaining 94.22% of its capacity even after 2000 charge−discharge cycles at a current density of 5 mA cm⁻². Furthermore, this Cu doped Fe₂O₃/g-C₃N₄ composite electrode demonstrated impressive electrochemical performance, boasting a specific capacitance of 244.0 F g⁻¹ and an impressive maximum energy density of 5.31 W h kg⁻¹ at a scan rate of 5 mV s⁻¹. These findings highlight the substantial potential of the Cu doped Fe₂O₃/g-C₃N₄ electrode for supercapacitor applications.

1. Introduction

Supercapacitors have emerged as a promising solution for addressing the increasing energy demands and environmental concerns associated with non-renewable energy sources.[1,2] These electrochemical capacitors offer numerous advantages over traditional batteries, including superior lifespan, high power density, cost-effectiveness, rapid charging/discharging rates, and enhanced safety.[3,4] Supercapacitors are classified as either an Electrical Double Layer Capacitor (EDLC) or a pseudocapacitor based on their charge storage method.[5,6] The electrochemical performance of the electrode materials substantially influences the efficiency of supercapacitors.[7,8] In recent years, there has been a growing interest in flexible energy storage devices, particularly in the field of wearable electronics. Among these devices, fiber-shaped supercapacitors have gained significant attention due to their lightweight nature, small size, and high flexibility.[9] However, conventional supercapacitors do not meet the requirements of flexible energy storage devices due to their weight, bulkiness, and low capacitance.[10,11] Consequently, researchers are focusing on the development of electrode materials with high specific capacitance and stability to enhance the performance of supercapacitors. These materials mainly comprise carbon materials, conductive polymers, and transition metal oxides, and their continuous advancement holds vital importance in the research and development of supercapacitors.[12–14]

In recent years, transition metal oxides have garnered significant attention from researchers due to their remarkable properties, including unique crystal structure, low band gap, and exceptional electrochemical reactivity.[15] Notably, nanostructured transition metal oxides such as CuO, Fe₂O₃, Co₃O₄, NiO, and V₂O₅ have been investigated extensively, as they possess a higher specific surface area that facilitates enhanced

*a*MES Abasaheb Garware College, Pune, Maharashtra, India. E-mail: haripawar2010@gmail.com; dilipsatpute@yahoo.com

*b*MGV'S Arts, Science and Commerce College, Nashik, Maharashtra, India

*c*Amrutvahini College of Engineering, Ahmednagar, India

*d*D. Y. Patil University, Pune, Maharashtra, India

*e*JDPS College, SGB Amravati University, Amravati, Maharashtra, India

*f*Smt. R S College, SGB Amravati University, Amravati, Maharashtra, India

electrochemical reactions.[11,16,17] Consequently, these materials exhibit higher specific capacitances compared to their bulk counterparts. Among these oxides, iron oxide (Fe_2O_3) stands out as a promising electrode material for supercapacitor (SC) applications due to its desirable attributes such as low-cost, high capacity, non-toxic nature, eco-friendliness, and ease of synthesis.[18] However, the application of Fe_2O_3 in supercapacitors is constrained by its inadequate electrical conductivity and limited cycle stability,[19] which hinder its electrochemical reaction over prolonged periods. The electrical conductivity of the electrode material plays a crucial role in enhancing the specific capacitance, energy density, and cycle life of the supercapacitor. Doping with external impurities is a widely adopted strategy to improve the electrical conductivity of electrode materials. In the literature, various doping methods, such as fluorine,[20] titanium,[21] lithium,[22] manganese,[23] chromium,[24] nickel,[25] etc., have been successfully employed to enhance the electrical conductivity of the supercapacitor electrode material. Furthermore, to enhance the energy density and cycle life of Fe_2O_3-based supercapacitors, many studies have reported the use of combinations of Fe_2O_3 with carbon-based substances such as reduced graphene oxide (rGO), graphitic carbon nitride (g-C_3N_4), carbon nanotubes (CNTs), and porous carbon.[26–28] As an illustration, Zhang et al. synthesized a rGO/Fe_2O_3 composite via a simple hydrothermal method as the active material for screen-printing functional inks. The composite exhibited a high specific capacitance of 703.91 F g^{-1} at 1 A g^{-1}.[19] Wei et al. developed hollow acanthospheres (Fe_2O_3@C-HASs) on carbon cloth via a solvothermal process and self-sacrifice template, showcasing their potential as high-quality anode materials for asymmetric supercapacitors.[29] Amirabad et al. investigated the enhancement of supercapacitor efficiency by modifying binder-free electrodes using Zn-doped Fe_2O_3 on MoS_2@rGO nanosheets.[30] Zhong et al. introduced a novel supercapacitor material composed of CeO_2–Fe_2O_3 nanoparticles supported on a highly porous carbon framework (CeO_2–Fe_2O_3/C) with a remarkable specific capacitance of 803 F g^{-1} at 1 mV s^{-1}.[31] These reports have shed light on the potential for investigating these composites for their supercapacitor capabilities. However, there is a lack of extensive research on the utilization of Fe_2O_3/carbon-based composites as electrode materials for supercapacitors. Consequently, our focus has been on synthesizing Cu-Fe_2O_3/g-C_3N_4 composites and exploring their application in supercapacitors.

In this investigation, we utilized a cost-effective and efficient hydrothermal technique to synthesize a distinctive Cu-Fe_2O_3/g-C_3N_4 composite material. The Fe_2O_3/g-C_3N_4 composition remained constant, with a specific focus on evaluating the influence of Cu doping in the Fe_2O_3 component. g-C_3N_4, synthesized through combustion, was introduced during the hydrothermal process, providing a nuanced approach for a comprehensive analysis of interactions and structural characteristics in the resulting material. The characterization of these composites was conducted using various analytical techniques such as XRD, FESEM, EDX, XPS, UV, and TEM. The Cu-Fe_2O_3/g-C_3N_4 composite material, prepared through the aforementioned method, was employed as an electrode in

supercapacitors. Remarkably, it displayed a specific capacitance of approximately 244 F g^{-1} at a scan rate of 5 mV s^{-1}. Furthermore, the composite exhibited only a 5.78% loss in specific capacitance after 2000 cycles, indicating its remarkable electrochemical stability. The Cu-Fe_2O_3/g-C_3N_4 electrode material prepared in this work offers substantial potential as an extraordinary option for uses in the field of supercapacitors due to its good specific capacitance.

2. Experimental

2.1 Synthesis of g-C_3N_4

Graphitic carbon nitride (g-C_3N_4) was prepared using equivalent amounts of urea and thiourea through a combustion method.[32] In the process of synthesizing g-C_3N_4, equal amounts of urea and thiourea (5 grams each) were combined in a mortar and pestle before being transferred to a silica crucible. The mixture was then heated to 550 °C for 5 hours using a muffle furnace set at a heating rate of 5 °C. The resulting yellow product was collected and utilized in the fabrication of the Cu-Fe_2O_3/g-C_3N_4 samples.

2.2 Synthesis of Cu doped Fe_2O_3@g-C_3N_4 nanocomposite

The synthesis of a Cu doped Fe_2O_3@g-C_3N_4 nanocomposite was performed using the hydrothermal method. Notably, the g-C_3N_4 component employed in the composite was prepared beforehand using a combustion synthesis approach. The first step in the synthesis involved preparing a 1 M solution of iron(III) nitrate nonahydrate in water and a 1 M solution of copper chloride in water. In a typical preparation procedure, 50 mg of g-C_3N_4 was initially dispersed in 40 mL of water under magnetic stirring this g-C_3N_4 was synthesized in combustion method and used in the synthesis of composite. Then, an appropriate amount of the copper salt solution and iron salt solution was added to this solution, and the mixture was stirred at room temperature for 10 minutes. Afterward, 0.2 M NaOH was added dropwise to the mixture while stirring it at 60 °C on a hot plate
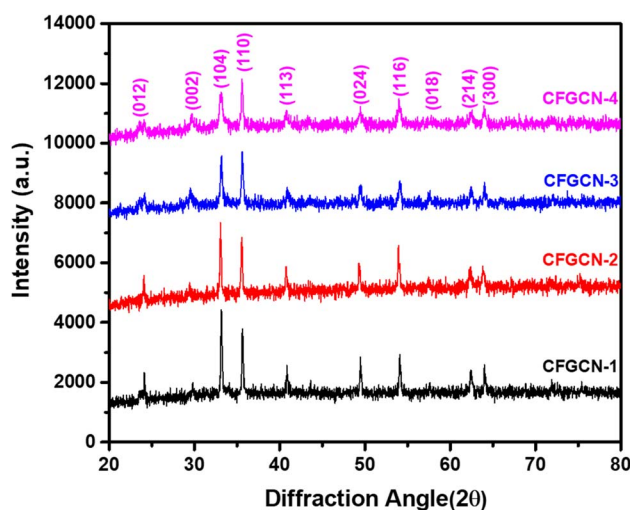

Fig. 1 XRD pattern of as-synthesized Cu doped Fe_2O_3@g-C_3N_4 nanocomposites.

for 2 hours. Once all the NaOH was added, the reaction mixture was cooled to room temperature while continuing to stir. Subsequently, the mixture was transferred to a hydrothermal container and placed in an oven at 160 °C for 12 hours. The autoclave was then allowed to cool naturally to ambient temperature. The resulting precipitate was collected, centrifuged, washed, and dried in a 55 °C oven. The dry product was then calcined for 4 hours at 550 °C. This process was repeated for different compositions of the Cu doped Fe_2O_3@g-C_3N_4 nanocomposite, specifically 0%, 2%, 4%, 6%, and 8% Cu doping, which were labelled as CFGCN-0, CFGCN-1, CFGCN-2, CFGCN-3, and CFGCN-4, respectively. The nanocomposites were subsequently characterized using various techniques. Table ESI 1† provides a summary of the different preparation conditions for the Cu doped Fe_2O_3@g-C_3N_4 nanocomposite.

2.3 Characterization

X-ray diffraction was utilized to identify the phase of a composite material comprising Cu doped Fe_2O_3@g-C_3N_4. A Philips diffractometer was employed with X-ray radiation at a wavelength of 1.540 Å at room temperature. X-ray photoelectron spectra were captured using a Prevac XPS system designed for ambient pressure. It featured a VG Scienta SAX 100 emission controller monochromator and an Al Ka anode with an energy of 1486.6 eV in transmission lens mode. The morphology analysis of the composite could be conducted using the JEOL JSM-7600F, FEG-SEM. Transmission electron microscopy (TEM) images of the synthesized product were obtained with a JEOL JEM-2200 FS Transmission Electron Microscope equipped with a field emission gun. Optical investigation was carried out using a Shimadzu model 1800 UV-visible spectrophotometer.

2.4 Electrochemical measurements

The electrodes were created using stainless steel (SS) plates, specifically of grade 304.0, as the foundational material. These SS plates were meticulously cleaned according to well-established laboratory standards. To remove pre-existing contamination on the stainless steel (SS) substrate, the
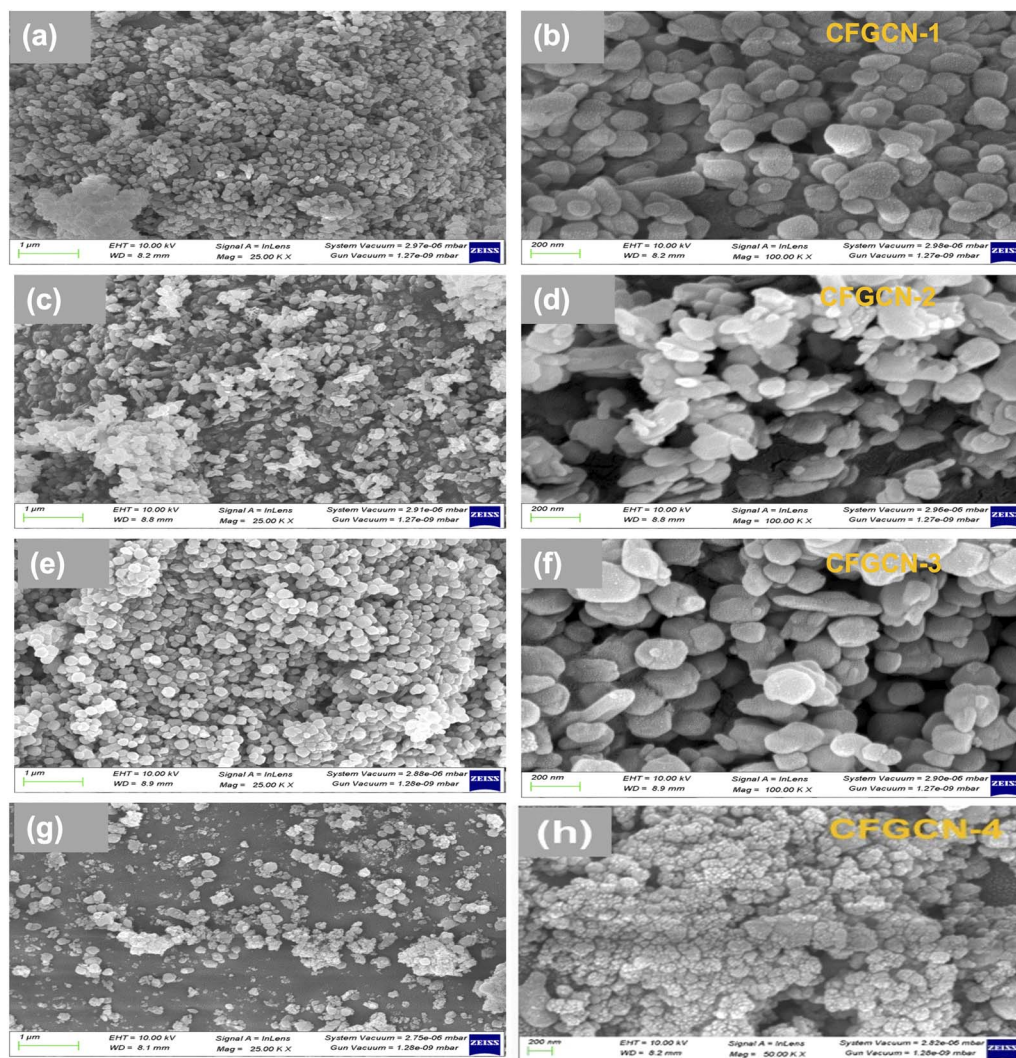

Fig. 2 FESEM images of (a) and (b) 2% Cu doped Fe_2O_3@g-C_3N_4 (CFGCN-1), (c) and (d) 4% Cu doped Fe_2O_3@g-C_3N_4 (CFGCN-2), (e) and (f) 6% Cu doped Fe_2O_3@g-C_3N_4 (CFGCN-3), and (g) and (h) 8% Cu doped Fe_2O_3@g-C_3N_4 (CFGCN-4).

substrate was first cleaned in detergent. It was then immersed in a 4 N HNO$_3$ solution for 45 min. The SS was simultaneously washed using acetone and distilled water and then dried in an oven at 55 °C. To craft the electrodes, we followed a widely-documented procedure outlined in existing literature.[33] To prepare the electrodes, a mixture consisting of acetylene black (AcB) and polyvinylidene fluoride (PVDF), each making up 5%

of the total weight, was combined with 90% of the as-prepared samples labelled as CFGCN-0, CFGCN-1, CFGCN-2, CFGCN-3, and CFGCN-4. This amalgamation took place in a solution of dimethylformamide (DMF). Subsequently, this blend was evenly spread using a doctor blade and left to dry at a temperature of 60 °C for a duration of 12 hours. The resulting electrodes were then employed for the purpose of conducting
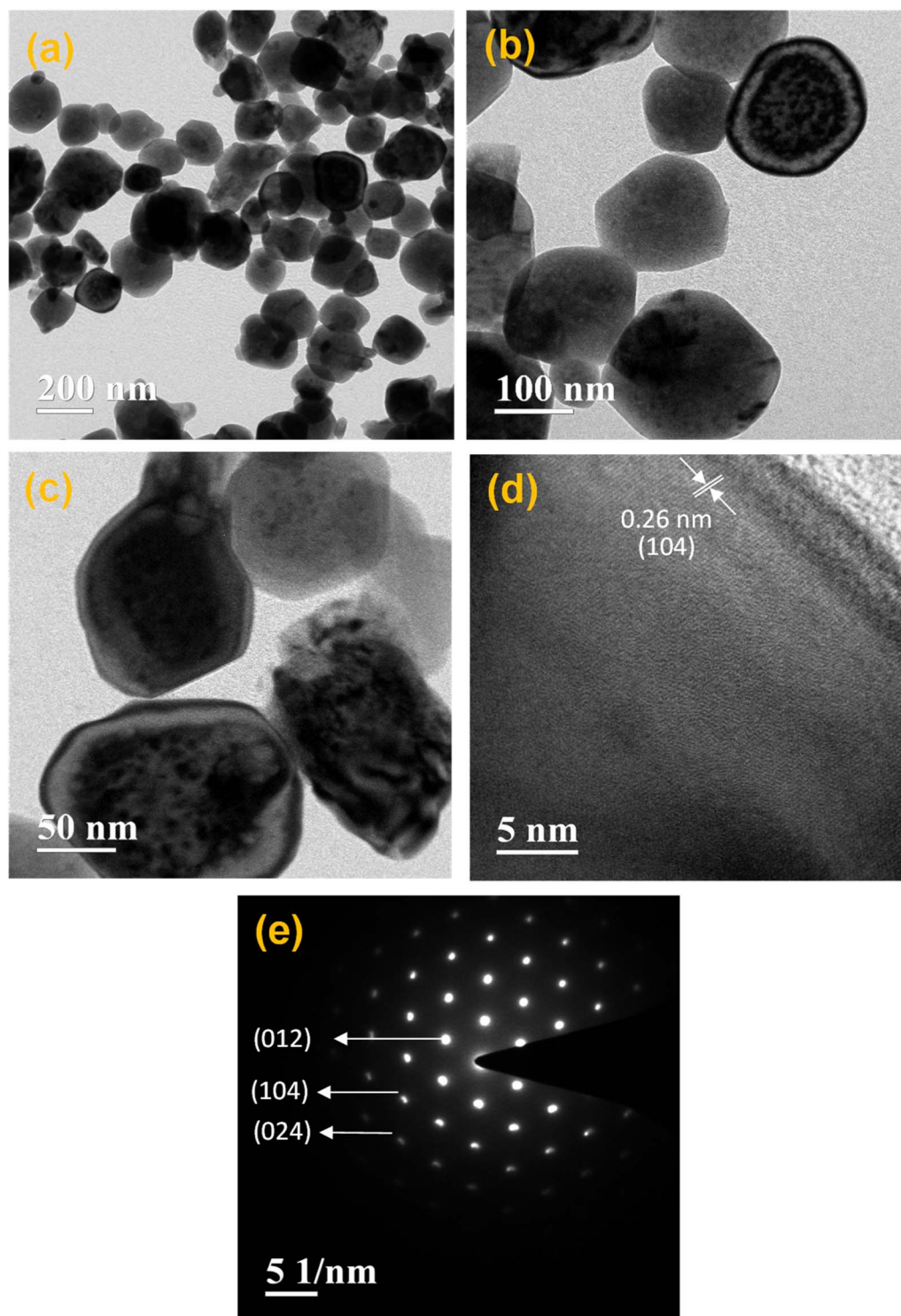

Fig. 3 (a)–(c) TEM images, (d) HRTEM image, and (e) the SAED pattern of 6% Cu doped Fe$_2$O$_3$@g-C$_3$N$_4$ (CFGCN-3).

electrochemical analysis. The electrochemical supercapacitor properties of the electrodes, specifically those identified as CFGCN-0, CFGCN-1, CFGCN-2, CFGCN-3, and CFGCN-4, were evaluated through various methods, including cyclic voltammetry (CV), galvanostatic charge/discharge (GCD), and electrochemical impedance spectroscopy (EIS).

3. Results and discussion

The study conducted a powder X-ray diffraction (XRD) analysis to assess the phase purity and crystalline structure of three materials: as-prepared g-C_3N_4, pristine Fe_2O_3, and Cu doped Fe_2O_3@g-C_3N_4 nanocomposite. The XRD pattern for g-C_3N_4 and
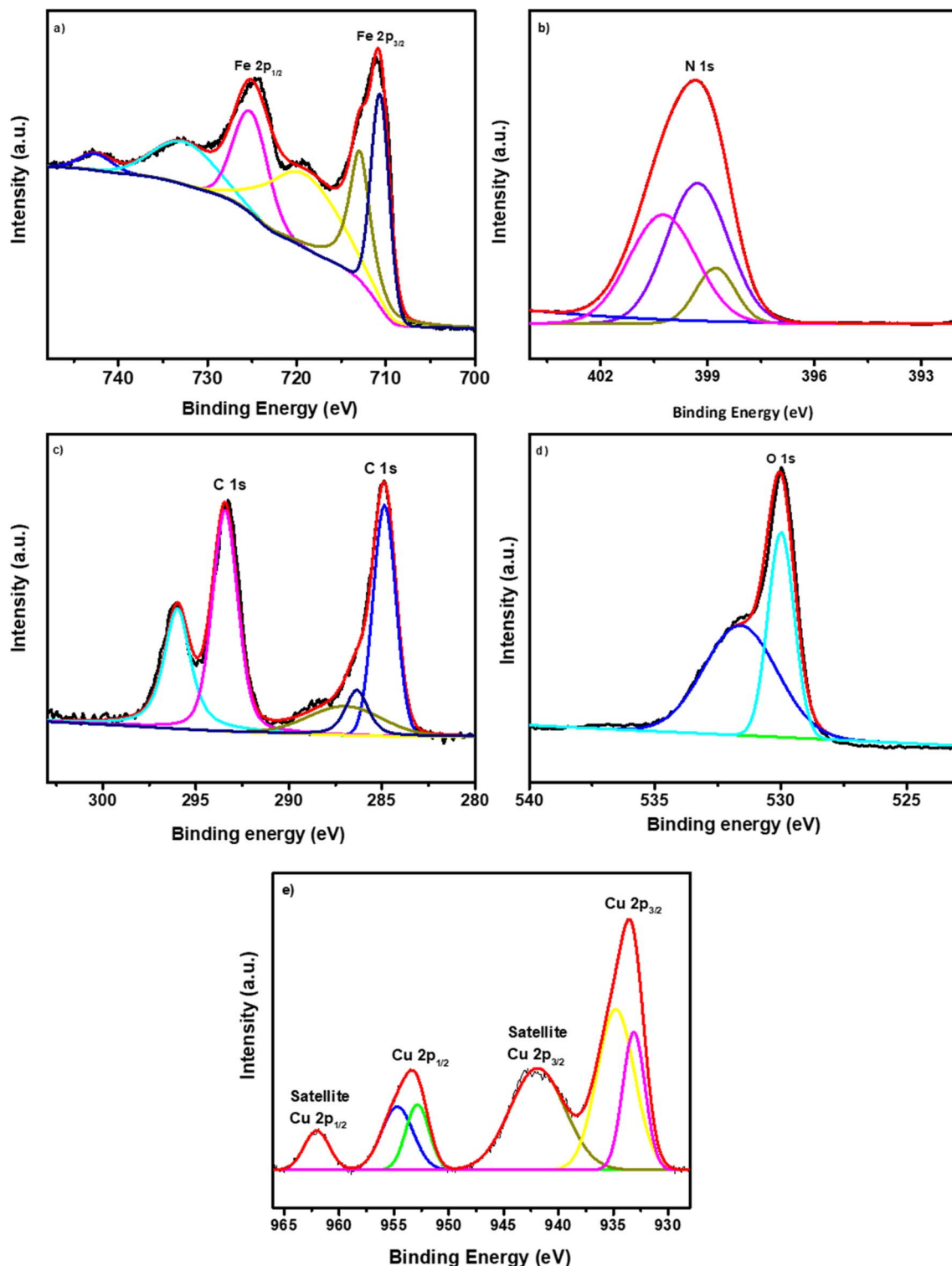

Fig. 4 XPS spectra of 6% Cu doped Fe_2O_3@g-C_3N_4 (CFGCN-3) (a) Fe 2p (b) N 1s (c) C 1s (d) O 1s and (e) Cu 2p.

Fe_2O_3 was consistent with previous literature findings, serving as a foundation for this extended research (Fig. ESI-1†).[32] The X-ray diffraction patterns for the newly synthesized Cu doped Fe_2O_3@g-C_3N_4 nanocomposites are presented in Fig. 1. In the XRD pattern of pristine g-C_3N_4, a peak was observed at 29.64°, corresponding to the (002) stacking layered structure, in agreement with JCPDS card no. 87-1526.[32] Additionally, diffraction peaks at 23.63°, 33.03°, 35.38°, 40.56°, 49.36°, 53.85°, 57.69°, 62.53°, and 63.92° were identified and indexed to lattice planes (012), (104), (110), (113), (024), (116), (018), (214), and (300), respectively. The XRD patterns for all Cu doped Fe_2O_3@g-C_3N_4 nanocomposites exhibited diffraction peaks corresponding to both Fe_2O_3 and g-C_3N_4, indicating the successful formation of Cu doped Fe_2O_3@g-C_3N_4 nanocomposites.[34] It is noteworthy that all samples exhibited crystalline phases, suggesting that the introduction of copper through doping had a minimal impact on the crystal structure of Fe_2O_3. However, heavily doped copper led to a slightly reduced particle size, as evidenced by a broadened peak with reduced intensity in the case of CFGCN-4. Importantly, no diffraction peaks associated with impurities were observed in any of the composites, underscoring the formation of highly pure Cu doped Fe_2O_3@g-C_3N_4 nanocomposites.

The morphology of Cu doped Fe_2O_3@g-C_3N_4 nanocomposites was examined through field emission scanning electron microscopy (FESEM), and Fig. 2 displays both low and high magnification FESEM images of these nanocomposites, denoted as CFGCN-1 to CFGCN-4. Pristine g-C_3N_4 exhibited its characteristic layered structure with wrinkles, as depicted in Fig. ESI 2.† In contrast, the Fe_2O_3@g-C_3N_4 nanocomposites displayed irregularly shaped nanostructures. The same morphological characteristics were observed in the Cu doped Fe_2O_3@g-C_3N_4 nanocomposites. Specifically, the surface morphology of CFGCN-1 revealed irregular shapes and some nearly spherical, prematurely aggregated nanostructures with a reduced diameter compared to the Fe_2O_3@g-C_3N_4

nanocomposite (Fig. 2a and b). Fig. 2c and d illustrate FESEM images of CFGCN-2, showing a mixed morphology comprising irregularly shaped nanostructures of varying sizes and the deposition of nanoparticles atop them. CFGCN-3, as shown in Fig. 2e and f, displayed fully developed irregularly shaped nanostructures, clearly indicating that copper played a crucial role in the formation of these well-developed structures. Furthermore, when the copper content exceeded 6%, as depicted in Fig. 2g and h, the fully developed irregular nanostructures tended to aggregate. This distortion in morphology is likely attributed to an increase in *in situ* pressure during the hydrothermal synthesis process. In a nutshell, optimal copper doping led to the formation of highly crystalline, well-developed irregularly shaped nanostructures.

In order to ascertain the elemental composition of both the as-synthesized pristine g-C_3N_4 and the Cu doped Fe_2O_3@g-C_3N_4 nanocomposites, Energy Dispersive Spectra (EDS) analysis was conducted. In Fig. ESI 3a,† the spectrum for pristine g-C_3N_4 displays distinct peaks corresponding to the elements carbon (C) and nitrogen (N). Conversely, Fig. ESI 3b–3e† reveal EDS spectra for the ferrites CFGCN-1, CFGCN-2, CFGCN-3, and CFGCN-4, showcasing prominent peaks corresponding to the elements copper (Cu), carbon (C), nitrogen (N), iron (Fe), and oxygen (O). Notably, the absence of any impurity peaks in the spectra provides confirmation of the high purity of these samples.

The investigation of the microstructure of a nanocomposite consisting of 6% Cu doped Fe_2O_3@g-C_3N_4 was conducted using transmission electron microscopy (TEM), as depicted in Fig. 3. The examination revealed the presence of fully developed irregularly shaped nanostructures, with an average diameter of approximately 120 nm. This observation aligns well with the findings from field-emission scanning electron microscopy (FESEM) shown in Fig. 2e and f. Furthermore, Fig. 3d displays lattice fringes with a spacing of 0.26 nm, corresponding to the (104) lattice plane of Fe_2O_3. The selected area electron
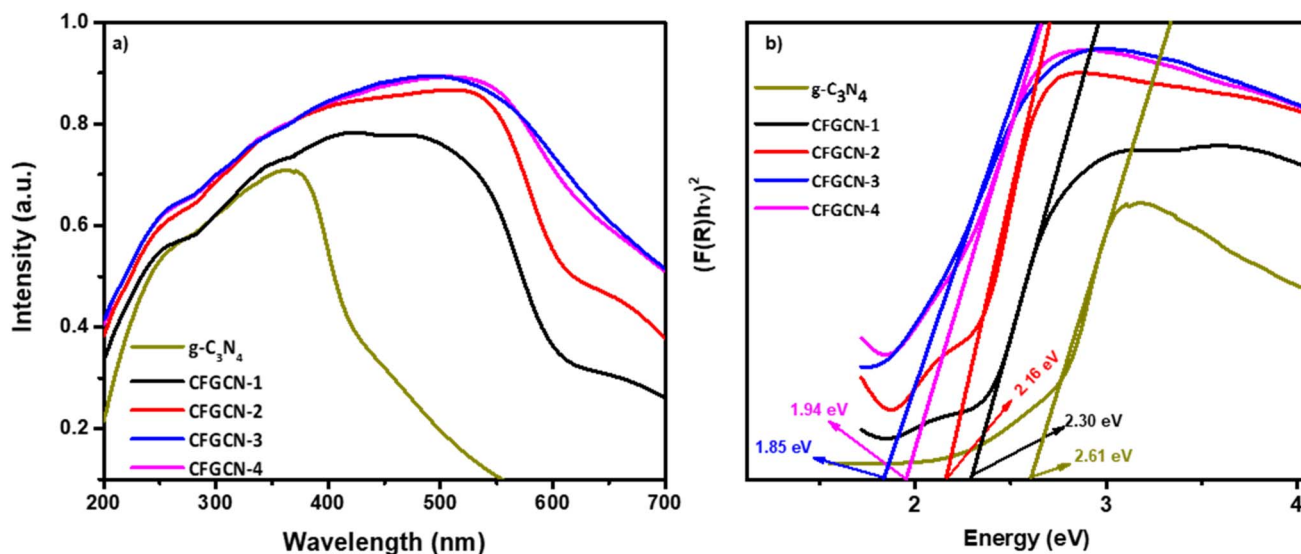

Fig. 5 (a) UV-vis absorption spectra and (b) Kubelka–Munk function verses energy of g-C_3N_4 and Cu-Fe_2O_3@g-C_3N_4 nanocomposites.

diffraction (SAED) pattern of the 6% Cu doped Fe_2O_3@g-C_3N_4 nanocomposite, as shown in Fig. 3e, clearly indicates its crystalline nature. The SAED pattern reveals the presence of crystalline planes such as (012), (104), and (024), consistent with the X-ray diffraction (XRD) results. This correspondence between

the TEM and XRD results confirms the structural characteristics of the CFGCN-3 nanocomposite.

The chemical composition of the as-synthesized nanocomposite, consisting of 6% Cu doped Fe_2O_3@g-C_3N_4, was confirmed using X-ray photoelectron spectroscopy. The survey
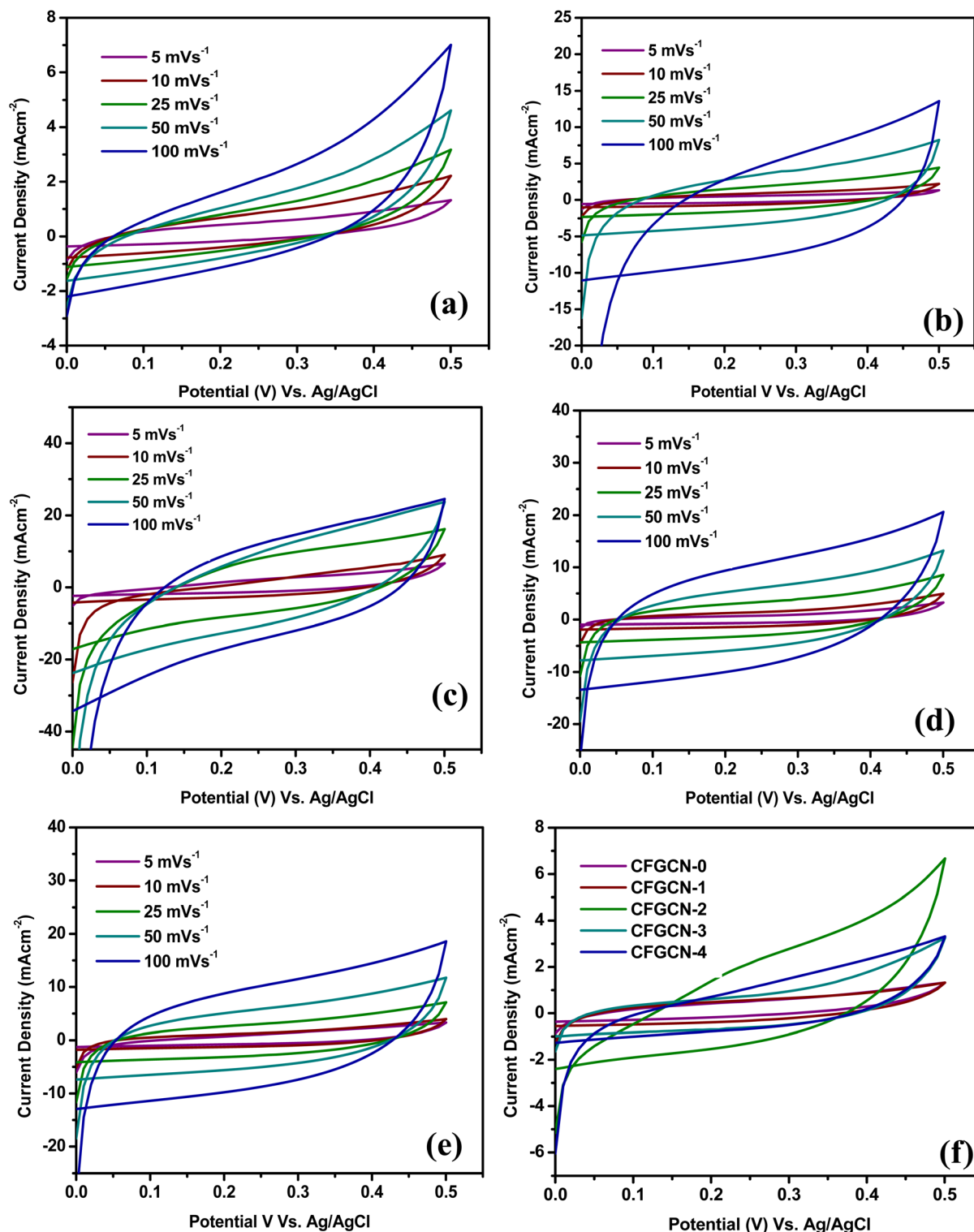

Fig. 6 Cyclical Voltammetry (CV) curves for (a) CFGCN-0, (b) CFGCN-1, (c) CFGCN-2, (d) CFGCN-3, and (e) CFGCN-4 samples in 1 M Na_2SO_4 solution at various scan rates, and (f) comparative CV curves of all samples at a current density of 5 mV s^{-1}.

spectra of this nanocomposite revealed the presence of Cu, Fe, O, N, and C elements, thereby substantiating the chemical makeup of the synthesized sample (as shown in Fig. ESI 4†). In Fig. 4a–f, high-resolution spectra for Fe 2p, N 1s, C 1s, O 1s, and Cu 2p elements are presented. The Fe 2p doublet in Fig. 4a exhibited clear splitting into two components: one at a binding energy of 710.80 eV, corresponding to Fe $2p_{3/2}$, and the other at 724.33 eV, corresponding to Fe $2p_{1/2}$.[35] In addition to these, two satellite peaks related to Fe 2p were observed in CFGCN-3, positioned at 719.06 eV and 733.22 eV.[36] Fig. 4b displays the high-resolution spectra of N 1s with a binding energy of 399.44 eV. This peak was further deconvoluted into three distinct peaks, which were assigned to the C–N–H, N–C$_3$, and C–N–C groups found in the triazine rings of g-C$_3$N$_4$.[37] The high-resolution spectra of C 1s, as depicted in Fig. 4c, revealed the presence of commonly observed peaks attributed to C–(N)$_3$ and C–C bonding within the g-C$_3$N$_4$ lattice, respectively.[38] As shown in Fig. 4d, the O 1s spectra demonstrated a predominant peak at 529.98 eV, which was attributed to oxygen lattice structures firmly established in the Fe$_2$O$_3$ crystal. Further deconvolution revealed two minor peaks at 531.98 eV and 530.19 eV, which could be ascribed to adsorbed oxygen species, most likely arising from C=O–Fe and C–O–Fe interactions.[39] The high-resolution Cu 2p spectrum (Fig. 4e) of CFGCN-3 displayed peaks at 933.54 and 953.47 eV, corresponding to Cu $2p_{3/2}$ and Cu $2p_{1/2}$, respectively. Additionally, two satellite peaks associated with Cu 2p in CFGCN-3 were observed at 942.15 eV and 962.44 eV.[40] These findings further substantiate the formation of the Cu doped Fe$_2$O$_3$@g-C$_3$N$_4$ nanocomposite.

Fig. 5a displays the UV-visible absorption spectra of pristine g-C$_3$N$_4$ and Cu doped Fe$_2$O$_3$@g-C$_3$N$_4$ nanocomposites (CFGCN-1 to CFGCN-4). In the spectra, the absorption edge at 475 nm is characteristic of pristine g-C$_3$N$_4$, a feature well-documented in the literature.[41] Notably, the absorption curves of the Cu doped Fe$_2$O$_3$@g-C$_3$N$_4$ nanocomposites closely resemble those of pristine g-C$_3$N$_4$, but with greater intensity and a shift toward longer wavelengths. This broadened absorbance and the bathochromic shift distinctly indicate the successful incorporation of copper into the Fe$_2$O$_3$@g-C$_3$N$_4$ nanocomposites.[42] Furthermore, the band energy of as-synthesized pristine g-C$_3$N$_4$ and Cu doped Fe$_2$O$_3$@g-C$_3$N$_4$ nanocomposites was evaluated using Kubelka–Munk function as shown in Fig. 5b. The estimated band gap of g-C$_3$N$_4$, CFGCN-1, CFGCN-2, CFGCN-3, and CFGCN-4 were observed to be 2.61 eV, 2.30 eV, 2.16 eV, 1.84 eV and 1.94 eV respectively. Moreover, as the copper content varies from 2% to 6%, the extent of the bathochromic shift in the Cu doped Fe$_2$O$_3$@g-C$_3$N$_4$ nanocomposites progressively increases, affirming higher levels of copper doping. However, at 8% copper doping in the Fe$_2$O$_3$@g-C$_3$N$_4$ nanocomposites (CFGCN-4) a further increase in the band gap was observed.

Fig. 6(a–e) display the cyclic voltammetry (CV) curves for electrodes CFGCN-0, CFGCN-1, CFGCN-2, CFGCN-3, and CFGCN-4, each evaluated at various scan rates ranging from 5 to 100 mV cm^{-2} within a potential window of 0–0.5 V (*versus* Ag/AgCl). What's immediately apparent is the classic pseudocapacitive behavior in all these electrodes, suggesting the occurrence of Faradaic reactions. Intriguingly, Fig. 6(f) reveals a notable

difference in the area under the CV curve, with CFGCN-3 demonstrating a significantly larger area compared to the other electrodes at a current density of 5 mV s^{-1}. To quantify this, specific capacitance values were calculated for all the electrodes at different scan rates, and the results are summarized in Table 1. Among all the samples, CFGCN-2 stood out with the highest specific capacitance of 244.0 F g^{-1} and an energy density of 5.21 W h kg^{-1} at a scan rate of 5 mV s^{-1}.

To understand the charge–discharge characteristics, galvanostatic charge–discharge (GCD) studies were performed within the potential range of 0–0.5 V *versus* Ag/AgCl in a 1 M Na$_2$SO$_4$ electrolyte. Fig. 7(a–e) illustrate the GCD curves for CFGCN-0, CFGCN-1, CFGCN-2, CFGCN-3, and CFGCN-4 electrodes at different current densities ranging from 1 to 5 mA cm^{-2}. Once again, CFGCN-3 displayed a remarkable performance with an extended discharge time (as shown in Fig. 7(f)). Quantitative values of specific capacitance calculated from GCD curves of studied samples at different current densities (1–5 mA cm^{-2}) are summarized in Table 2. Notably, CFGCN-2 exhibited the highest specific capacitance of 191.1 F g^{-1} and the highest energy density of 6.7 W h kg^{-1}, surpassing the performance of the other electrodes. The effective application of the Cu-doping approach is highlighted in this study to enhance the electrochemical performance by augmenting the electrical conductivity of the ferrite material. Among all examined electrodes, the superior electrochemical performance of CFGCN-3 is attributed to the optimal doping of Cu within the Fe$_2$O$_3$ crystal lattice and its proper integration with g-C$_3$N$_4$.[22,34]

Furthermore, the variation in specific capacitance with scan rate is evident in Fig. 8(a). Fig. 8(b) illustrates the changes in specific capacitance with current density. When compared to the specific capacitance and energy density values obtained at lower current densities, it is noticeable that at higher current densities, the specific capacitance and energy density values tend to decrease. This decrease can be attributed to the diminished accessibility of electrolyte ions at higher scan rates and current densities. CFGCN-3 demonstrates superior performance compared to other electrodes at low current levels; however, its efficacy diminishes at higher current levels, rendering it the least effective under such conditions. This phenomenon is attributed to the fact that, at lower current density values, the electrolyte ions have sufficient time to permeate the pores within the electrode material. As a result, a substantial number of electrolyte ions can fill the pores

Table 1 Determination of specific capacitance from cyclic voltammetry (CV) at various scan rates for electrodes of samples CFGCN-0, CFGCN-1, CFGCN-2, CFGCN-3, and CFGCN-4

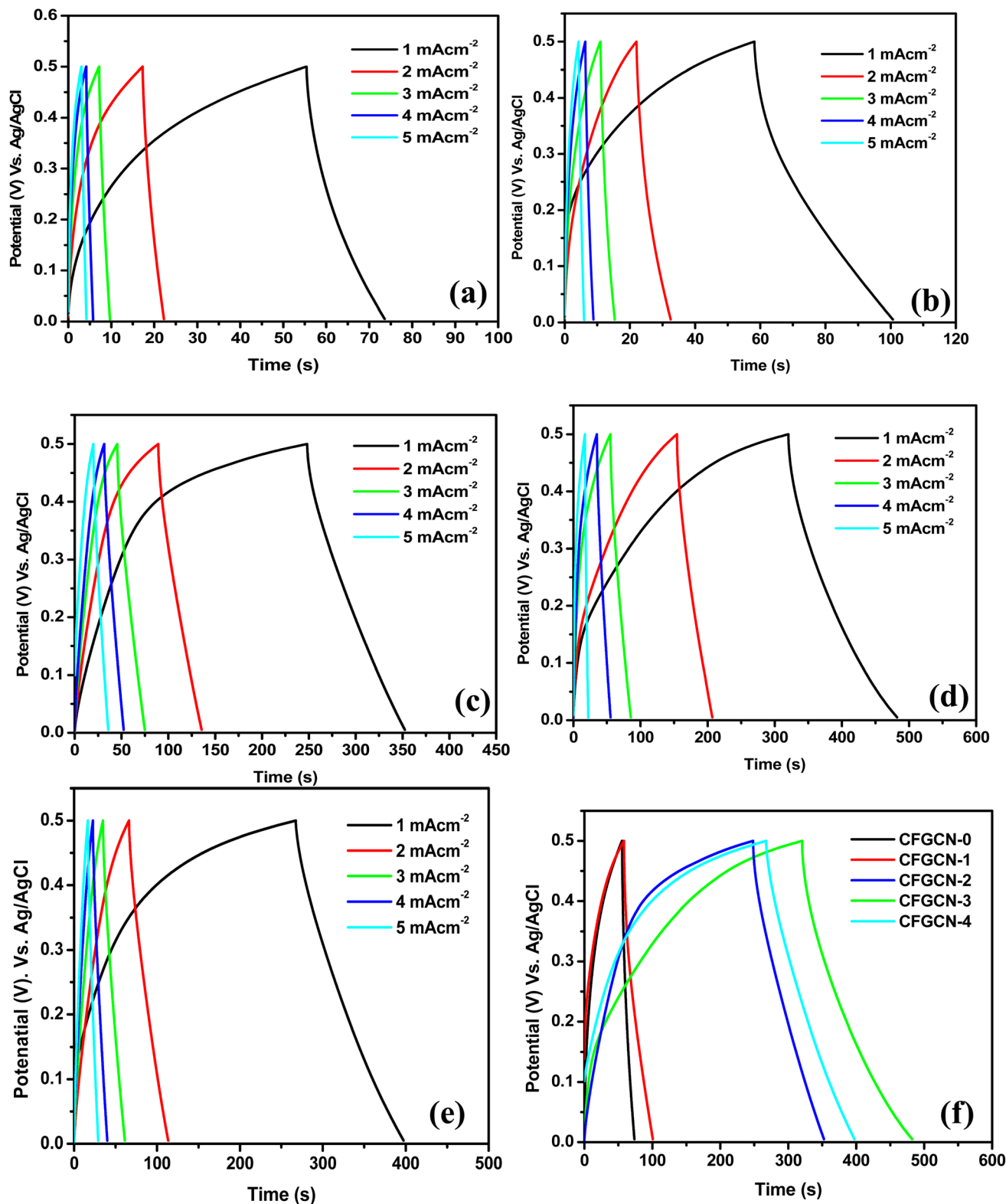| Scan rate (mV s^{-1})	Specific capacitance (F g^{-1})				
	CFGCN-0	CFGCN-1	CFGCN-2	CFGCN-3	CFGCN-4
5	48.8	67.6	124.8	244.0	129.0
10	45.0	59.8	116.3	171.7	104
25	23.5	51.9	103.8	142.0	95.7
50	16.3	51.3	84.28	130.4	88.1
100	12.28	38.2	78.01	90.2	75.5

Fig. 7 GCD curves of the (a) CFGCN-0, (b) CFGCN-1, (c) CFGCN-2 (d) CFGCN-3, (e) CFGCN-4 samples in 1 M Na_2SO_4 solution at scan rates ranging 1 to 5 mA cm^{-2}, and (f) GCD curves of all samples (CFGCN-0, CFGCN-1, CFGCN-2, CFGCN-3, and CFGCN-4) at constant current density of 1 mA cm^{-2}.

present on the electrode surface. Conversely, at higher current density values and high scan rates, the electrolyte ions struggle to access all the pores on the electrode surface. Consequently, the electrode exhibits lower electrochemical performance, particularly when compared to its performance at lower current densities. The outstanding electrochemical performance of

Table 2 Specific capacitance obtained from GCD curves for CFGCN-0, CFGCN-1, CFGCN-2, CFGCN-3, and CFGCN-4 sample electrodes at a constant current density of 1 mA cm^{-2}

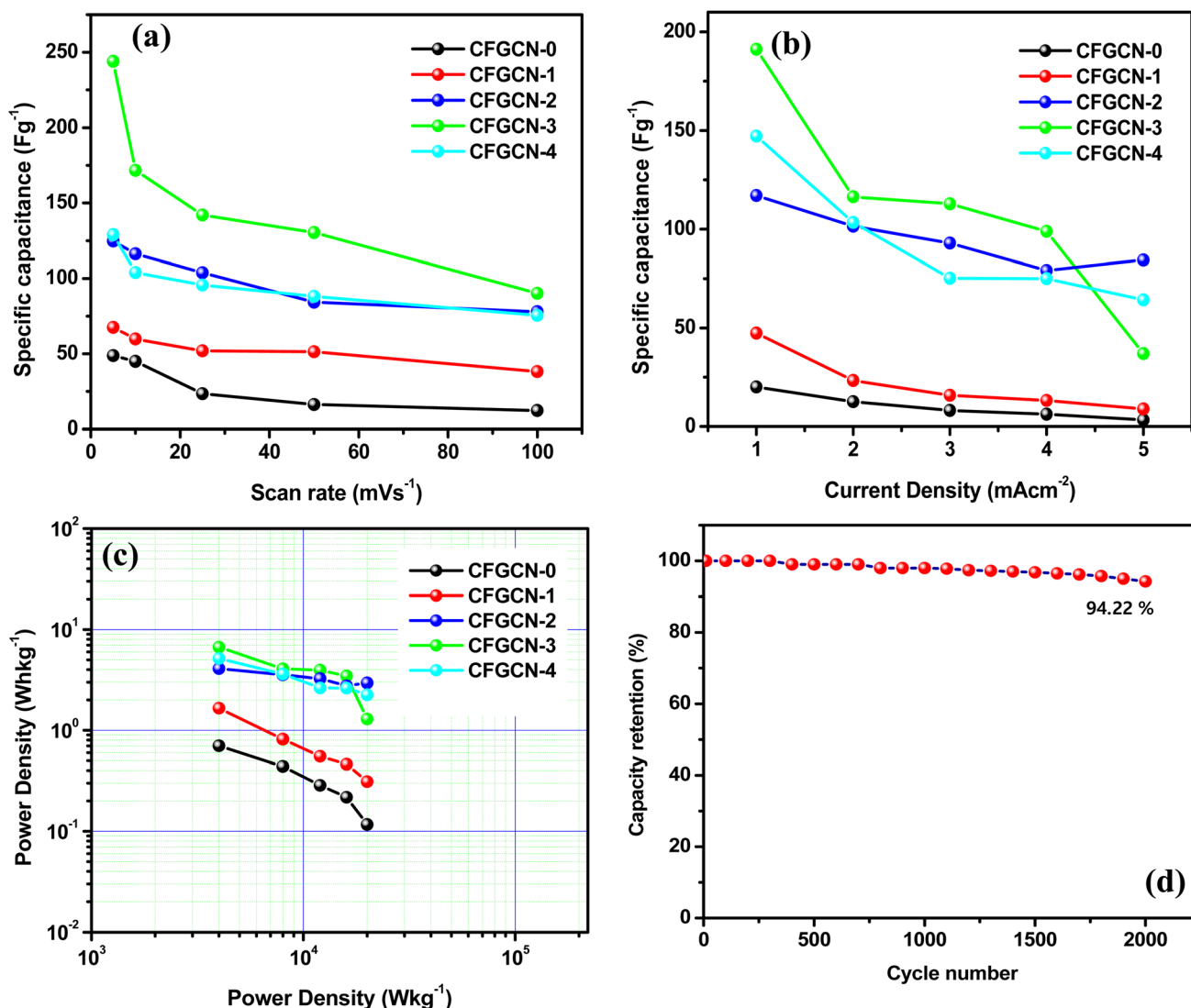| Current density (mA cm^{-2})	Specific capacitance (F g^{-1})				
	CFGCN-0	CFGCN-1	CFGCN-2	CFGCN-3	CFGCN-4
1	20.07	47.36	117.06	191.11	147.22
2	12.53	23.33	101.51	116.40	103.40
3	8.17	15.80	92.93	112.83	75.17
4	6.22	13.20	79.07	98.93	75.02
5	3.33	8.89	84.41	72.61	64.22

Fig. 8 (a) Variation specific capacitance *vs.* scan rate, (b) variation specific capacitance with current densities, (c) Ragone plot and (d) coulombic efficiency of CFGCN-3 samples at constant current density of 5 mA cm^{-2}.

CFGCN-3 can be attributed to multiple factors, including its larger surface area, uniform porosity, appropriate doping, excellent electrical conductivity, and efficient ion insertion/extraction processes during the charging and discharging cycles. A Ragone plot in Fig. 8(c) highlights the energy and power density performance of the different sample electrodes, emphasizing the impressive performance of CFGCN-2 and CFGCN-3. Moreover, Fig. 8(d) illustrates the remarkable 94.22% capacity retention of the CFGCN-3 electrode over 2000 charge–discharge cycles at a consistent current density of 5 mA cm^{-2}, underlining its suitability for high-energy-density supercapacitors (Table 3).

Table 3 Comparison of our work with related studies in the literature

Electrode material	Method of synthesis	Electrolyte	Sp. capacitance (F g^{-1}), scan rate (mV s^{-1})/ current density (A g^{-1})	Columbic efficiency (%) & cycles	Ref.
Fe_2O_3	Chemical bath deposition	1 M NaOH	178 F g^{-1}, 5 mV	89% & 3000	43
α-Fe_2O_3	Self-assembly process	0.5 M Na_2SO_3	127 F g^{-1}, 1 A g^{-1}	80% & 1000	44
α-Fe_2O_3	Hydrothermal approach	1 M KOH	249 F g^{-1}	93.6% & 2000	45
α-Fe_2O_3/rGO	Hydrothermal method	1 M KOH	255 F g^{-1}, 0.5 A g^{-1}	90% & 4000	46
Cu-Fe_2O_3/g-C_3N_4	Hydrothermal method	1 M Na_2SO_4	244.0 F g^{-1}, 5 mV s^{-1}	94.22% & 2000	In the present work
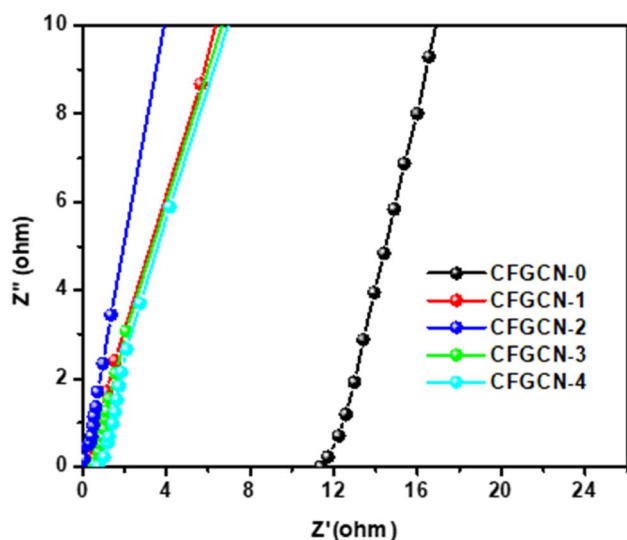
Fig. 9 EIS spectra for CFGCN-0, CFGCN-1, CFGCN-2, CFGCN-3, and CFGCN-4 samples.

Table 4 The values of R_{ct} and R_s obtained for sample (CFGCN-0, CFGCN-1, CFGCN-2, CFGCN-3, and CFGCN-4) electrode

Sample code	R_{ct} (ohm)	R_s (ohm)
CFGCN-0	12.04	18.56
CFGCN-1	1.56	2.6
CFGCN-2	0.956	1.54
CFGCN-3	0.78	1.66
CFGCN-4	0.88	1.25

combination of Cu-Fe_2O_3 within g-C_3N_4. The findings derived from the EIS spectra align with those obtained from cyclic voltammetry (CV) and galvanostatic charge–discharge (GCD) curves, underscoring the consistency of our results. In summary, the EIS analysis offered crucial insights into the electrochemical behavior of these samples, emphasizing the significance of low R_{ct} and R_s values in achieving enhanced electrochemical performance, and highlighting CFGCN-3 as a standout candidate in this regard, owing to its unique composition and properties.

Electrochemical impedance spectroscopy (EIS) analysis was conducted to investigate the charge transfer resistance (R_{ct}) and solution resistance (R_s) at the electrode–electrolyte interface for various electrode samples, including CFGCN-0, CFGCN-1, CFGCN-2, CFGCN-3, and CFGCN-4. This analysis was performed within a frequency range of 10.0–0.001 kHz using a 1 M Na_2SO_4 electrolyte, with a constant perturbation potential of 5 mV. The resulting Nyquist plot (Fig. 9) provided valuable insights into the electrochemical properties of these samples. From the Nyquist plot, the R_{ct} and R_s values for each sample were determined based on the high and low-frequency regions, respectively, and are summarized in Table 4. Notably, CFGCN-0 exhibited the highest R_{ct} and R_s values when compared to the other samples. It's important to highlight that elevated R_{ct} and R_s values can adversely impact the overall electrochemical performance of the electrode within the electrolyte. Conversely, CFGCN-3 displayed the lowest R_{ct} and R_s values among all the samples. This characteristic sets CFGCN-3 apart, indicating a superior electrochemical performance. As a consequence, CFGCN-3 demonstrated a higher energy density, specific capacitance, and an extended cycle life. These outcomes can be attributed to the excellent electrical conductivity of CFGCN-3, appropriate Cu doping into Fe_2O_3, and the optimal

4. Conclusion

In this present study, we successfully synthesized a Cu doped Fe_2O_3@g-C_3N_4 nanocomposite through a hydrothermal process. Our investigation focused on examining the impact of varying levels of copper doping on the material's morphology and electrochemical properties. The Cu doped Fe_2O_3@g-C_3N_4 composite electrode, comprising 6% Cu doped Fe_2O_3 in conjunction with g-C_3N_4, exhibited remarkable characteristics. Notably, it displayed exceptional cycling stability, retaining 94.22% of its capacity even after undergoing 2000 charge–discharge cycles at a current density of 5 mA cm^{-2}. Furthermore, this electrode demonstrated impressive electrochemical performance, boasting a specific capacitance of 244.0 F g^{-1} and a remarkable maximum energy density of 5.31 W h kg^{-1} at a scan rate of 5 mV s^{-1}. These enhanced electrochemical properties can be attributed to several factors, including its morphology, appropriate doping levels, excellent electrical conductivity, and efficient ion insertion/de-insertion processes during charging and discharging. Therefore, these compelling results firmly establish the Cu doped Fe_2O_3@g-C_3N_4 electrode as a highly promising material for supercapacitor applications, highlighting its potential in energy storage and related technologies.

Conflicts of interest

The authors declare that they have no known competing financial interests or personal relationships that could have appeared to influence the work reported in this paper.

Acknowledgements

References

1 L. Zhang, Y. Tian, C. Song, H. Qiu and H. Xue, *J. Alloys Compd.*, 2021, **859**, 157816.

2 I. Rabani, R. Zafar, K. Subalakshmi, H.-S. Kim, C. Bathula and Y.-S. Seo, *J. Hazard. Mater.*, 2021, **407**, 124360.

3 L. Zhong, C. Wu, S. Lei, G. Liang, S. Sayyar, B. Gao and L. Lin, *ACS Appl. Energy Mater.*, 2022, **5**, 8004–8014.

4 S. D. Balgude, S. S. Barkade and S. P. Mardikar, *Multifunctional Nanostructured Metal Oxides for Energy Harvesting and Storage Devices*, 2020, pp. 169–194.

5 J. Tan, Z. Li, M. Ye and J. Shen, *ACS Appl. Mater. Interfaces*, 2022, **14**, 37259–37269.

6 S. Sahoo, R. Kumar, E. Joanni, R. K. Singh and J.-J. Shim, *J. Mater. Chem. A*, 2022, **10**, 13190–13240.

7 R. A. Mir, S. Upadhyay, R. A. Rather, S. J. Thorpe and O. P. Pandey, *Energy Adv.*, 2022, **1**, 438–448.

8 P. Tiwari and D. Janas, *Mater. Chem. Front.*, 2022, **6**, 2386–2412.

9 Y. Zhao, D. Dong, Y. Wang, S. Gong, T. An, L. W. Yap and W. Cheng, *ACS Appl. Mater. Interfaces*, 2018, **10**, 42612–42620.

10 Y. Shi, L. Sun, Y. Zhang, H. Si, C. Sun, J. Gu, Y. Gong, X. Li and Y. Zhang, *J. Alloys Compd.*, 2021, **853**, 156903.

11 S. A. Delbari, L. S. Ghadimi, R. Hadi, S. Farhoudian, M. Nedaei, A. Babapoor, A. Sabahi Namini, Q. V. Le, M. Shokouhimehr, M. Shahedi Asl and M. Mohammadi, *J. Alloys Compd.*, 2021, **857**, 158281.

12 J. Hu, B. Gao, Q. Qi, Z. Zuo, K. Yan, S. Hou and D. Zou, *ACS Omega*, 2022, **7**, 31628–31637.

13 J. Gu, L. Sun, Y. Zhang, Q. Zhang, X. Li, H. Si, Y. Shi, C. Sun, Y. Gong and Y. Zhang, *Chem. Eng. J.*, 2020, **385**, 123454.

14 A. Zaka, K. Hayat and V. Mittal, *ACS Appl. Electron. Mater.*, 2021, **3**, 574–596.

15 A. K. Lichchhavi and P. M. Shirage, *J. Energy Storage*, 2022, **55**, 105692.

16 M. Kandasamy, S. Sahoo, S. K. Nayak, B. Chakraborty and C. S. Rout, *J. Mater. Chem. A*, 2021, **9**, 17643–17700.

17 C. Liang, S. Wang, S. Sha, S. Lv, G. Wang, B. Wang, Q. Li, J. Yu, X. Xu and L. Zhang, *J. Mater. Chem. C*, 2023, **11**, 4288–4317.

18 Y. Zhu, S. Cheng, W. Zhou, J. Jia, L. Yang, M. Yao, M. Wang, J. Zhou, P. Wu and M. Liu, *ACS Sustain. Chem. Eng.*, 2017, **5**, 5067–5074.

19 X. Zhang, Y. Pei, B. Tian, Y. Wu, G. Tang, Q. Liu, J. Liang and W. Wu, *J. Energy Storage*, 2022, **56**, 106136.

20 K. Karthikeyan, S. Amaresh, S. N. Lee, V. Aravindan and Y. S. Lee, *Chem.– Asian J.*, 2014, **9**, 852–857.

21 Y. Zeng, Y. Han, Y. Zhao, Y. Zeng, M. Yu, Y. Liu, H. Tang, Y. Tong and X. Lu, *Adv. Energy Mater.*, 2015, **5**, 1402176.

22 A. M. Tamboli, M. S. Tamboli, S. K. Shinde, J. Byeon, N. T. N. Truong, C. Kim and C. Park, *J. Alloys Compd.*, 2022, **928**, 167242.

23 J. Zhang, Y. Wang, H.-J. Liao, T.-Y. Yang, Z. Chen, X. Yan, Z. Zhou, H. lv, W.-W. Liu and Y.-L. Chueh, *Mater. Today Energy*, 2020, **17**, 100388.

24 M. Aalim, I. Irshad, A. M. Tantray, A. Sohail, B. Want and M. Shah, *J. Mater. Sci.: Mater. Electron.*, 2023, **34**, 1409.

25 P. Agale, V. Salve, K. Patil, S. Mardikar, S. Uke, S. Patange and P. More, *Ceram. Int.*, 2023, **49**, 27003–27014.

26 Y. Tian, X. Hu, Y. Wang, C. Li and X. Wu, *ACS Sustain. Chem. Eng.*, 2019, **7**, 9211–9219.

27 L. Liu, J. Wang, C. Wang and G. Wang, *Appl. Surf. Sci.*, 2016, **390**, 303–310.

28 L. Yue, S. Zhang, H. Zhao, M. Wang, J. Mi, Y. Feng and D. Wang, *J. Alloys Compd.*, 2018, **765**, 1263–1266.

29 Y. Wei, C.-M. Zhou, X.-M. Cao, Z.-J. Sun, Q. Wu, D.-L. Liu, Z. Xing and Q.-G. Zhang, *J. Alloys Compd.*, 2022, **929**, 167245.

30 T. N. Amirabad, A. A. Ensafi and B. Rezaei, *Fuel*, 2022, **330**, 125645.

31 H. Zhang, L. Xia, J. Tang, Y. Li, L. Wang, C. Ouyang and S. Zhong, *Mater. Adv.*, 2022, **3**, 6818–6825.

32 S. Balgude, S. Godase, A. Shinde and C. Harak, *Curr. Res. Green Sustainable Chem.*, 2021, **4**, 100210.

33 S. J. Uke, V. P. Akhare, S. P. Meshram and G. N. Chaudhari, *Adv. Sci., Eng. Med.*, 2018, **10**(12), 1174–1182.

34 V. V. Pham, T. K. Truong, L. V. Hai, H. P. P. La, H. T. Nguyen, V. Q. Lam, H. D. Tong, T. Q. Nguyen, A. Sabbah, K.-H. Chen, S.-J. You and T. M. Cao, *ACS Appl. Nano Mater.*, 2022, **5**, 4506–4514.

35 S. Balgude, K. Patil, S. Moharil, M. Puranik, S. Kadam, P. Lokhande, S. Patange and P. More, *ChemistrySelect*, 2022, **7**, e202200221.

36 A. Rajan, M. Sharma and N. K. Sahu, *Sci. Rep.*, 2020, **10**, 15045.

37 C. Harak, D. Satpute, V. Kadam, N. Kolhe, A. Wade, S. Balgude, S. Mardikar, S. Balgude and H. Pawar, *Emergent Mater.*, 2023, **6**, 1797–1807.

38 T. J. Al-Musawi, R. Asgariyan, M. Yilmaz, N. Mengelizadeh, A. Asghari, D. Balarak and M. Darvishmotevall, *Magnetochemistry*, 2022, **8**, 137.

39 X. Shi, X. Li, G. Liu, M. Du, J. Zhang, G. Liu and Q. Lu, *J. Mater. Sci.*, 2020, **55**, 10035–10046.

40 Z. Jin, C. Liu, K. Qi and X. Cui, *Sci. Rep.*, 2017, **7**, 39695.

41 X. Guo, J. Duan, C. Li, Z. Zhang and W. Wang, *J. Mater. Sci.*, 2020, **55**, 2018–2031.

42 K. Jangam, S. Balgude, H. Pawar, S. Patange and P. More, *Surf. Interfaces*, 2022, **33**, 102189.

43 P. M. Kulal, D. P. Dubal, C. D. Lokhande and V. J. Fulari, *J. Alloys Compd.*, 2011, **509**, 2567–2571.

44 S. Shivakumara, T. R. Penki and N. Munichandraiah, *ECS Electrochem. Lett.*, 2013, **2**, A60.

45 X. Zheng, X. Yan, Y. Sun, Y. Yu, G. Zhang, Y. Shen, Q. Liang, Q. Liao and Y. Zhang, *J. Colloid Interface Sci.*, 2016, **466**, 291–296.

46 Y. Zhu, S. Cheng, W. Zhou, J. Jia, L. Yang, M. Yao, M. Wang, J. Zhou, P. Wu and M. Liu, *ACS Sustain. Chem. Eng.*, 2017, **5**, 5067–5074.